

Elliptical phantoms for tomographic reconstruction

Sub-pixel image processing report

Tom Szwagier^{1,2}

1. ENS Paris-Saclay, Gif-sur-Yvette, France,
2. Mines Paris, Paris, France,
tom.szwagier@minesparis.psl.eu

Abstract

The reconstruction of an object sub-structure using measurements of physical quantities such as the density of protons in Magnetic Resonance Imaging (MRI) or the tissues X-ray attenuation coefficients in Computed Tomography (CT scan) is a challenging inverse problem. One has to carefully choose the measurements parameters in order to avoid creating artifacts on the reconstructed image that could impact the analysis of the imaged structure and lead to a misdiagnosis. To that extent, researchers have been performing simulations on objects whose structure is perfectly known – referred to as *phantoms* – in order to study the relationship between the acquisition parameters and the reconstruction resolution. However, a common mistake happens in the simulation of the acquisition step, where the measures are performed numerically, on a discrete version of the original continuous object instead of the object itself, either by lack of a closed-form analytical expression for the object itself and the operator leading to its measurements, or simply by ignorance. This mistake, known as *inverse crime*, harms the simulation of the reconstruction process and can lead to overly optimistic results. In this paper, we design an elliptical phantom and derive several analytical formulas related to its tomographic reconstruction, with a critical look at the inverse crime situation. Those formulas are then implemented for visual interpretation. We are aware that the contributions from this work might be limited given how advanced is the field of tomographic reconstruction; the idea of this project was simply to use the knowledge from the Sub-pixel image processing course in order to analyze a new image acquisition framework.

Keywords: Tomography, Phantom, Inverse Crime, Medical Image acquisition

1 Introduction

Medical images are acquired through the measurement of biological quantities.

- In the case of Magnetic Resonance Imaging (MRI), we measure the density of protons through a magnetic field, that causes the 1H atoms to align with it. A radio frequency pulse then modifies the longitudinal and transversal magnetization and the resulting signal, characteristic of the global density of protons, is measured via receiving coils (**Brown et al. 2014**). A magnetic field gradient is used to control the parameters of the magnetic field, and the resulting signal can be expressed in terms of Fourier Transform of the local density of protons, that belong to a mathematical space commonly referred to as *k-space*.
- In the case of Computed Tomography (CT scan) we measure the variation of intensity of X-rays that irradiate the structure of the patient that we want to image, due to the absorption by the organs that depends on their attenuation coefficient (**Herman 2009**). Same as for MRI, the measures are global, and we perform them this time at several angles in order to retrieve the local density.

The outputs of the acquisition are then used to reconstruct the source image, using an inverse problem formulation.

- For MRI, the number of Fourier coefficients acquired is finite, so we have discrete K-space measurements (most of the time Cartesian or in spiral) so we cannot directly use Inverse Fourier Transform to recover the original image. Instead, we use an inverse problem formulation, like Total Variation (TV) regularization (**Rudin, Osher, and Fatemi 1992**), or more recently Shannon Total Variation (**Abergel and Moisan 2017**), which uses a continuous regularization term in the loss based on the gradient of the Shannon interpolation of the image to reconstruct.
- For CT scan, we use Fourier slice theorem (Theorem 1) that states that the original local density can be reconstructed using the global rays intensity variations at every angle. However, in practice, we have as well as for MRI only a finite number of angular measurements, the reconstructed object will only be an approximation of the original object.

In both cases, the parameters of the acquisition highly impact the quality of the reconstruction, where *quality* refers to the faithfulness with respect to the original object shape and non-uniformity. The less measurements we have, the lowest the resolution is and we risk to miss some important elements of the imaged structure, like tiny cancerous cells in brain CT scans. Therefore, it is of major importance to study the link between the acquisition resolution and the output reconstruction resolution, in order not to miss some important details when analyzing the image, especially given that doctors can already make some diagnosis errors on perfectly well acquired images.

A method to analyze the impact of the measurements distribution on the quality is to perform simulations on objects whose compositions are fully known – referred to as *phantoms* – so that we are able to quantitatively compare the output of the reconstruction algorithm to the input, depending on the acquisition parameters. From those objects, we have to compute first the outputs of the simulated medical image acquisition (Fourier Transforms for MRI, line integrals for CT scan), and second the reconstruction from those measures.

However, a classical mistake (voluntary or not) is to simulate the acquisition process on the wrong object, like a rasterized image, or even on a rasterized version of a continuous image, which can clearly suffer from sampling issues, like aliasing, especially for medical images that consist of superposition of solid components, which lead to discontinuities and thus high frequencies that make Shannon theorem hypotheses not respected (**Guerquin-Kern et al. 2012**). This situation, known as *inverse crime* (**Colton and Kress 1992**) and famous in inverse problems theory, can be a major problem and paradoxically lead to artificially good results of reconstruction. Indeed, the output discrete image can be close to the rasterized version of the input image, but suffers from aliasing, and then misses some important parts of the original input image.

In order to avoid that situation, researchers have been developing continuous phantoms, whose parameters are fully known, so that they can get the true measures that they would get in the imaging setting,

using analytical formulas, and not numerical approximations on the rasterized version of the phantom. The famous first contribution was Shepp and Logan's phantom, an ellipse-based phantom (**Larry A. Shepp and Logan 1974**). Then researchers came up with more sophisticated phantoms with the time, trying to get closer to true subjects, with more complex shapes and density distributions (**Koay, Sarlls, and Özarslan 2007; Guerquin-Kern et al. 2012**).

In several of those articles, analytical formulas are derived for the phantom as well as some quantities linked to it (Fourier Transform for instance), and those phantoms are then used to study the impact of the parameters on MRI reconstruction and to illustrate the inverse crime situation.

In this paper, we design an ellipse-based phantom, and lead a detailed analysis of the CT reconstruction process by deriving analytical formulas for each of the steps in the reconstruction. The inverse crime situation is also considered, in order to study the impact of the sampling of a continuous input object on the reconstruction. The obtained equations, although sometimes very complex, open some paths to convergence analysis with respect to the discretization step, and are then implemented and illustrated through several tomography experiments that testify of the formulas correctness.

We are aware that this work might not yield any contribution to the tomographic reconstruction field, as it is already well developed. The idea of this project was simply to use the tools from the *Sub-pixel Image Processing* course in order to lead a mathematical and critical analysis of an image acquisition process that differs from the camera model studied in the course. For this purpose, we did not lead an extensive bibliographical research in the tomographic reconstruction domain. We simply read some related articles to get a basic understanding of the field, and then used the knowledge from the course to carry out our calculations. Here follows a brief literature review to situate and motivate our work.

1.1 Related works

Analytical phantoms [**Larry A. Shepp and Logan 1974**] introduce an ellipse-based phantom with 11 ellipses and study the impact of the parameters on the reconstruction, from a general theoretical point of view, and apply it to a single regular ellipse.

[**L. Shepp et al. 1980**] introduce a more sophisticated 3D phantom with 17 ellipses and provide their exact coordinates for reproducibility. It is not actually the main point of the article, which is to prove that computerized tomography can be applied to Nuclear Magnetic Resonance (NMR) imaging as well, getting called NMR Computerized Tomography (NCT), and benefits from time resolution advantages over classical direct methods like the ones cited previously (Fourier coefficients). NMR has several advantages over X-ray CT because it is non-invasive and non-ionizing.

[**Koay, Sarlls, and Özarslan 2007**] base their work on the latter article's 3D phantom and introduce a better formulated and more intuitive representation of the coordinates for reproducibility. Their most important contribution is the derivation of the analytical formulas for the Fourier coefficients of the 3D phantom with sinusoidal and polynomial functions only, and not any Bessel function, using some advanced formulas from spherical wave functions theory.

[**Guerquin-Kern et al. 2012**] show the limits of elliptical-based phantoms in their simplicity, and propose a way more complex 2D model, using both ellipses and piecewise-polynomial boundaries (including spline, Bézier contours and polygons), as well as taking into account the MRI receiving-coil sensitivities, which is useful for parallel MRI experiments (cf. [**Pruessmann et al. 1999**]).

Inverse Crime The same authors [**Guerquin-Kern et al. 2012**] put in perspective the inverse crime situation, which consists in using the same rasterized image for both simulation of the medical image acquisition experiment and reconstruction, yielding overly optimistic results on the reconstruction. They explain indeed that rasterized images – especially *medical* ones, which have a lot of discontinuities – suffer from aliasing, and thus reconstruction using them as input and getting good reconstruction scores will yield aliased images as well, potentially missing some important features of the true continuous input image.

[**Abergel and Moisan 2017**] introduce a Shannon theory-based Total Variation (TV) reconstruction from sparse Fourier coefficients, in the compressed sensing setup, that can be useful to model MRI acquisition experiments. The model uses a continuous regularization term in the loss based on the gradient of the Shannon interpolation of the image to reconstruct. They show that the simulation consisting in the

"mathematical" acquisition of the Fourier coefficients of a rasterized version of [Larry A. Shepp and Logan 1974]'s phantom using Discrete Fourier Transform (which by the way is not realistic because in the real world we get k-space coefficients by controlling the excitation signal) yields bad results in their Shannon Total Variation (STV) reconstruction, specifically because the input image is already aliased and doesn't respect Shannon sampling theorem, whereas the results with classical TV are good when compared to the discrete image. They solve that issue by introducing a non-aliased version of the sampled phantom, by low-pass filtering the 10-fold higher resolution phantom smoothed by a Gaussian filter). This time STV leads to way better results than TV reconstruction.

1.2 Contributions

The domain of medical image reconstruction is already very well developed and can quickly go out of the context of the course if we want to contribute actively to it. The aim of this project is to study the process of CT reconstruction from the point of view of continuous phantoms. Specifically, we will introduce a homemade 2D ellipse-based phantom, from which we will derive all the CT reconstruction analytical formulas, in order to study the influence of the sampling resolution on the reconstruction, both from a theoretical point of view, and a practical one, implementing all the formulas and illustrating the impact of the reconstruction parameters. Finally, we will formulate an inverse crime approach and study the impact of considering a discrete input image for the simulation on the reconstruction.

2 Prerequisites on Computed Tomography reconstruction

In the next section, we will consider an elliptical continuous phantom, and derive from it several formulas related to the Computed Tomography reconstruction method. For that purpose, let us begin to recall how the Computed Tomography reconstruction method works.

Tomography (Herman 2009) is a classical medical image reconstruction method. The name comes from the word *tomos* which means a *slice*, and the method consists in scanning several slices of a patient's body, and to use geometry and image processing to reconstruct the whole body from its slices. Tomography is a 3D method, hence the word *slice*, however here, for simplicity, we will consider 2D CT reconstruction from 1D rays. The idea between X-ray CT, which is the main method of CT, is the "photoelectric effect" [A. Becquerel, 1839; A. Einstein, 1905; M. Planck, 1900], which claims that the evolution of an X-ray's intensity passing through an object can be formulated as: $dI = -I(x)\rho(x)dx$, where $\rho(x)$ refers to the local X-ray attenuation coefficient of the irradiated object.

When we shoot a linear X-ray beam – parameterized by its slope and intercept – through a patient in order to image a sub-structure, the ray will go through a 1D slice of the patient, and the output intensity will be related to the X-ray attenuation coefficients along the line. A powerful theorem from [Kak and Slaney 2001] claims the following:

Theorem 1 (Fourier slice theorem) *The 1D Fourier transform of a parallel projection of an image $f(x, y)$ at an angle θ gives a slice of the two-dimensional transform $F(u, v)$, subtending an angle θ with the u -axis.*

The theorem is illustrated in Figure (1).

From that we can recover all the Fourier coefficients of an imaged patient's acquisition, and by Fourier inversion theorem, we can then recover the image itself.

More formally, this theorems makes intervene the Radon transform (Radon 1986, but the original publication dates back to 1917) of the distribution of attenuation coefficients, which is the line integral of a shot ray.

If the equation of the line is:

$$t = x \cos \theta + y \sin \theta \quad (1)$$

The the Radon transform of ρ at angle θ is:

$$\mathcal{R}_\theta(t) = \int_{\theta, t \text{ line}} \rho(t, s) ds \quad (2)$$

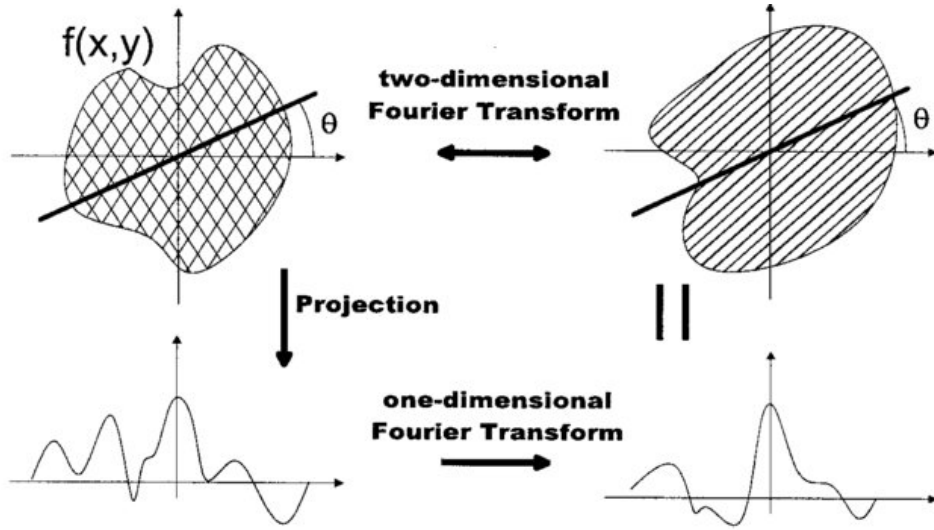


Figure 1: Illustration of the Fourier Slice Theorem (Ripoll, Kettunen, and Herzig 2002).

What we end up with is called a *sinogram*.
By definition its Fourier transform is:

$$S_\theta(\omega) = \int_{-\infty}^{-\infty} \mathcal{R}_\theta(t) e^{-i\omega t} dt = \int_{-\infty}^{+\infty} \left[\int_{\theta, t \text{line}} \rho(t, s) ds \right] e^{-i\omega t} dt \quad (3)$$

Which can be re-written using (1) as:

$$S_\theta(\omega) = \int_{-\infty}^{+\infty} \int_{-\infty}^{+\infty} \rho(x, y) e^{-i\omega(x \cos \theta + y \sin \theta)} dx dy \quad (4)$$

Which finally yields, by definition of the Fourier transform:

$$S_\theta(\omega) = F(\omega \cos \theta, \omega \sin \theta) \quad (5)$$

If we scan the patient with all possible couples of line parameters (θ, t) , we get by the Inverse Fourier Transform theorem the original attenuation coefficients' distribution, which is directly related to the patient's different organs, so we can get the position of the organs as well as their exact geometry.

However, in the real setting, like for image acquisition by a camera as seen in the course, we only irradiate the patient using a finite number values (θ, t) , so we end up with discrete values for the sinogram, which can therefore be considered as a discrete 2D image in our case, the horizontal axis being the t 's and the vertical axis being the θ 's, as illustrated in Figure (2).

The common discrete method consists in using Discrete Fourier Transform (DFT) on the sinogram values, for each row, yielding approximations of the radial Fourier transform at angles θ 's. Then interpolation is performed on that radial image, to get the estimated Cartesian Fourier coefficients, and then process back by Discrete Inverse Fourier Transform.

Of course, we can guess that the choice of discretization step is very important and highly impacts the reconstruction quality. In medical imaging, the quality of the reconstruction is of paramount importance, because otherwise one can miss important details of the imaged patients, like the presence of a tumor.

In this work, we will study the effects of that discretization from scratch, i.e. based only on the prerequisites on CT reconstructions explained in the current section and on the tools we were given in this course, without reading some articles that studied the theory of CT reconstruction. Indeed, the theory is so much vast that understating it would take a lot of time and actually contributing to it would be even harder.



Figure 2: Example of a discrete 2D sinogram

3 Methods

We previously described the CT reconstruction method. Now our idea was to study each step of this reconstruction process with the explicit example of an elliptical phantom, which has been irradiated with a finite number of (θ, t) rays, and compare the formulas to the ones obtained with the continuous phantom in order to try to detect patterns caused by the sampling, similarly to Shannon theorem.

We will first of all get the equations for the continuous phantom reconstruction with all the possible (θ, t) rays, then for the continuous phantom reconstruction with a limited number of (θ, t) , and finally we will illustrate the inverse crime situation, where we get the sinogram from a sampled version of the continuous phantom.

Given the linear nature of the operators, we can simply study one ellipse and sum the results for the full phantom.

3.1 Continuous reconstruction

3.1.1 Fourier Transform

Simple ellipse Let's first compute the formula for the Fourier transform of a simple uniform ellipse of density 1 with parameters (a, b) .

The absorption coefficient function can be written as:

$$\rho_{(a,b)}(x, y) = \begin{cases} 1 & \text{if } \left(\frac{x}{a}\right)^2 + \left(\frac{y}{b}\right)^2 \leq 1 \\ 0 & \text{otherwise} \end{cases} \quad (6)$$

Then one gets by definition of the Fourier Transform:

$$\hat{\rho}_{(a,b)}(k_x, k_y) = \int_{-\infty}^{+\infty} \int_{-\infty}^{+\infty} \rho_{(a,b)}(x, y) e^{-i(k_x x + k_y y)} dx dy \quad (7)$$

$$= \int_{\left(\frac{x}{a}\right)^2 + \left(\frac{y}{b}\right)^2 \leq 1} e^{-i(k_x x + k_y y)} dx dy \quad (8)$$

$$\left(X = \frac{x}{a}; Y = \frac{y}{b} \right) \quad (9)$$

$$= \int_{X^2 + Y^2 \leq 1} e^{-i(k_x a X + k_y b Y)} ab dX dY \quad (10)$$

$$(X = r \cos(\theta); Y = r \sin(\theta)) \quad (11)$$

$$= ab \int_{r=0}^1 r \left[\int_{\theta=0}^{2\pi} e^{-i(k_x a r \cos(\theta) + k_y b r \sin(\theta))} d\theta \right] dr \quad (12)$$

Now let's study the inner integral.

We use the following lemma¹:

$$\alpha \sin(x) + \beta \cos(x) = c \cos(x + \varphi) \quad (13)$$

with $c = \operatorname{sgn}(\alpha) \sqrt{\alpha^2 + \beta^2}$; $\varphi = \arctan\left(\frac{\beta}{\alpha}\right)$ if $\alpha \neq 0$.

Let's first suppose that $\alpha \neq 0$. One gets:

$$\int_{\theta=0}^{2\pi} e^{-i(k_x a r \cos(\theta) + k_y b r \sin(\theta))} d\theta = \int_{\theta=0}^{2\pi} e^{-i c \cos(\theta + \varphi)} d\theta \quad (14)$$

with $c = \operatorname{sgn}(k_x a r) \sqrt{(k_x a r)^2 + (k_y b r)^2} = \operatorname{sgn}(k_x) \sqrt{(k_x a)^2 + (k_y b)^2} r$; $\varphi = \arctan\left(\frac{k_y b}{k_x a}\right)$ if $k_x \neq 0$.

¹cf. [Wikipedia – List of trigonometric identities](#)

We use another lemma² on Bessel function that is:

$$J_n(x) = \frac{1}{2\pi} \int_{-\pi}^{\pi} e^{i(x \sin(\tau) - n\tau)} d\tau \quad (15)$$

One then gets, using periodicity arguments of the sinusoidal functions, as well as the 2π -long integration interval:

$$\int_{\theta=0}^{2\pi} e^{-ic \cos(\theta+\varphi)} d\theta = \int_{\theta=0}^{2\pi} e^{-ic \cos(\theta)} d\theta \quad (16)$$

$$= \int_{\theta=0}^{2\pi} e^{-ic \sin(\theta)} d\theta \quad (17)$$

$$= \int_{\theta=-\pi}^{\pi} e^{-ic \sin(\theta)} d\theta \quad (18)$$

$$= 2\pi J_0(-c) \quad (19)$$

Remark: As φ disappears from the integral for periodicity reasons, the case $\alpha = 0$ is valid as well *a posteriori*.

Now we can come back to our original calculus:

$$\hat{\rho}_{(a,b)}(k_x, k_y) = ab \int_{r=0}^1 r \left[\int_{\theta=0}^{2\pi} e^{-i(k_x ar \cos(\theta) + k_y br \sin(\theta))} d\theta \right] dr \quad (20)$$

$$= ab \int_{r=0}^1 r [2\pi J_0(-c)] dr \quad (21)$$

$$= ab \int_{r=0}^1 r \left[2\pi J_0 \left(-\operatorname{sgn}(k_x) \sqrt{(k_x a)^2 + (k_y b)^2} r \right) \right] dr \quad (22)$$

$$= 2\pi ab \int_{r=0}^1 r \left[J_0 \left(-\operatorname{sgn}(k_x) \sqrt{(k_x a)^2 + (k_y b)^2} r \right) \right] dr \quad (23)$$

$$= 2\pi ab \int_{r=0}^{-\operatorname{sgn}(k_x) \sqrt{(k_x a)^2 + (k_y b)^2}} \frac{r}{\left(-\operatorname{sgn}(k_x) \sqrt{(k_x a)^2 + (k_y b)^2} \right)^2} J_0(r) dr \quad (24)$$

$$= \frac{2\pi ab}{(k_x a)^2 + (k_y b)^2} \int_{r=0}^{-\operatorname{sgn}(k_x) \sqrt{(k_x a)^2 + (k_y b)^2}} r J_0(r) dr \quad (25)$$

$$= -\operatorname{sgn}(k_x) \frac{2\pi ab}{\sqrt{(k_x a)^2 + (k_y b)^2}} J_1 \left(-\operatorname{sgn}(k_x) \sqrt{(k_x a)^2 + (k_y b)^2} \right) \quad (26)$$

$$= -\operatorname{sgn}(k_x) \frac{2\pi ab}{\sqrt{(k_x a)^2 + (k_y b)^2}} - \operatorname{sgn}(k_x) J_1 \left(\sqrt{(k_x a)^2 + (k_y b)^2} \right) \quad (27)$$

$$\hat{\rho}_{(a,b)}(k_x, k_y) = 2\pi ab \frac{J_1 \left(\sqrt{(k_x a)^2 + (k_y b)^2} \right)}{\sqrt{(k_x a)^2 + (k_y b)^2}} \quad (28)$$

the two last lines being obtained using recurrence and parity properties of Bessel functions³.

²cf. Wikipedia – Bessel function

³cf. footnote 2; although parity was not explicitly evoked in the page, we deduced it by the first kind Bessel functions series expansion around $x = 0$ formula

Remark: If $k_x = 0, k_y = 0$, then $\hat{\rho}_{(a,b)}(k_x, k_y) = \int_{(\frac{x}{a})^2 + (\frac{y}{b})^2 \leq 1} dx dy = \mathcal{A}(\mathcal{E}(a, b)) = \pi ab$. Using first kind Bessel functions series expansion around $x = 0$ ⁴:

$$J_\alpha(x) = \sum_{m=0}^{+\infty} \frac{(-1)^m}{m! \Gamma(m + \alpha + 1)} \left(\frac{x}{2}\right)^{2m+\alpha} \quad (29)$$

we get that $J_1(x) \underset{x \rightarrow 0}{\sim} \frac{x}{2}$, so the formula still stands.

One finally gets the result:

$$\hat{\rho}_{(a,b)}(k_x, k_y) = 2\pi ab \frac{J_1\left(\sqrt{(k_x a)^2 + (k_y b)^2}\right)}{\sqrt{(k_x a)^2 + (k_y b)^2}} \quad (30)$$

More complex ellipse For our phantom, we will not simply use straight ellipses, but we will add rotations and translations. But that is not harder, we just need to add a previous change of variable, and the rest of the calculus will be the same.

Let $\mathcal{E}(a, b, \theta, r_0)$ be an ellipse of axes (a, b) , center $r_0 = (x_0, y_0)$ and which is added a rotation of angle θ .

Warning: The rotation must be done before the translation.

Then we can establish the mapping between the rotated and translated ellipse and the simple one: $r \rightarrow R(\theta)^T(r - r_0)$, with $R(\theta) = \begin{pmatrix} \cos(\theta) & -\sin(\theta) \\ \sin(\theta) & \cos(\theta) \end{pmatrix}$.

One gets:

$$\hat{\rho}_{(a,b,\theta,r_0)}(k) = \int_{r \in \mathcal{E}_{(a,b,\theta,r_0)}} e^{-ir \cdot k} dr \quad (31)$$

$$= \int_{u \in \mathcal{C}} e^{-i(r_0 + R(\theta)u) \cdot k} du \quad (32)$$

$$(r = r_0 + R(\theta)u) \quad (33)$$

$$= e^{-ir_0 \cdot k} \int_{u \in \mathcal{C}} e^{-i(R(\theta)u) \cdot k} dr \quad (34)$$

$$= e^{-ir_0 \cdot k} \int_{u \in \mathcal{C}} e^{-iu \cdot (R(\theta)^\top k)} dr \quad (35)$$

$$= e^{-ir_0 \cdot k} \hat{\rho}_{(a,b)}(R(\theta)^\top k) \quad (36)$$

$$= e^{-ir_0 \cdot k} |\text{diag}(a, b)| \left(2\pi \frac{J_1(\|\text{diag}(a, b)(R(\theta)^\top k)\|_2)}{(\|\text{diag}(a, b)(R(\theta)^\top k)\|_2)} \right) \quad (37)$$

where $\text{diag}(a, b) = \begin{pmatrix} a & 0 \\ 0 & b \end{pmatrix}$.

One finally gets the result:

$$\hat{\rho}_{(a,b,\theta,r_0)}(k) = 2\pi ab \cdot e^{-ir_0 \cdot k} \frac{J_1(\|\text{diag}(a, b)R(\theta)^\top k\|_2)}{(\|\text{diag}(a, b)R(\theta)^\top k\|_2)} \quad (38)$$

⁴cf. footnote 2

Comments: The non-compact support of Bessel functions introduces high-frequency components as it could have been expected from the discontinuity of the ellipse with respect to the background. The affine scaling by $\text{diag}(a, b)$ will create an elliptical Airy pattern with inverted axes with respect to the original ellipse. Indeed, if $a > b$, then the horizontal oscillations of the transformed Bessel function will be quicker than the vertical ones. The rotation of angle θ will yield a rotation with the same angle of the ellipse in the Fourier domain. The translation makes the up-to-now real Fourier Transform become complex, introducing a non piecewise constant phase.

Remark: When looking for a way to go from the simple ellipse to the rotated and translated one, we noticed that we could have simply first looked for the Fourier transform of a circle and then perform the mapping $r \rightarrow r_0 + R(\theta) \text{diag}(a, b)r$ from the disk to the rotated and translated ellipse. Then if we had a good memory, we would have remembered the classical result that the Fourier Transform of a disk can be expressed in terms of Bessel functions. At least it enabled us to manipulate some first kind Bessel properties, which would found themselves useful for the next computation of the Radon transform of an ellipse.

3.1.2 Radon transform

We will now compute the Radon transform of an ellipse. Like in the previous case, we will first compute it for a simple ellipse and then get the general formula using basic properties from the Radon transform.

Let's first of all parametrize the (θ, t) line from its equation. If (x, y) is such that

$$x \cos \theta + y \sin \theta = t \quad (39)$$

Then one has, on the orthogonal line, obtained by a rotation of $\frac{\pi}{2}$ in the counter-clockwise direction:

$$-x \sin \theta + y \cos \theta = z \quad (40)$$

for some $z \in \mathbb{R}$.

Fusing both equations gives a parametrization for the line:

$$\begin{cases} x = t \cos \theta - z \sin \theta \\ y = t \sin \theta + z \cos \theta \end{cases} \quad (41)$$

So the Radon transform can now be expressed as a 1D integral:

$$\mathcal{R}_\theta(t) = \int_{-\infty}^{+\infty} \rho(t \cos \theta - z \sin \theta, t \sin \theta + z \cos \theta) dz \quad (42)$$

$$= \int_{-\infty}^{+\infty} \mathbb{1}_{(x(z), y(z)) \in \mathcal{E}(a, b)}(z) dz \quad (43)$$

$$= \int_{-\infty}^{+\infty} \mathbb{1}_{\left((\frac{x(z)}{a})^2 + (\frac{y(z)}{b})^2 \leq 1\right)}(z) dz \quad (44)$$

$$= \int_{-\infty}^{+\infty} \mathbb{1}_{\left((\frac{t \cos \theta - z \sin \theta}{a})^2 + (\frac{t \sin \theta + z \cos \theta}{b})^2 \leq 1\right)}(z) dz \quad (45)$$

The set $\left\{ z \in \mathbb{R} \mid \left(\frac{t \cos \theta - z \sin \theta}{a}\right)^2 + \left(\frac{t \sin \theta + z \cos \theta}{b}\right)^2 \leq 1 \right\}$ is a segment of \mathbb{R} , whose bounds are the zeros of the polynomial

$$P(z) = \left(\frac{t \cos \theta - z \sin \theta}{a}\right)^2 + \left(\frac{t \sin \theta + z \cos \theta}{b}\right)^2 - 1 \quad (46)$$

$$= \left[\frac{\sin^2 \theta}{a^2} + \frac{\cos^2 \theta}{b^2}\right] z^2 + \left[2t \cos \theta \sin \theta \left(\frac{1}{b^2} - \frac{1}{a^2}\right)\right] z + \frac{t^2 \cos^2 \theta}{a^2} + \frac{t^2 \sin^2 \theta}{b^2} - 1 \quad (47)$$

The determinant is:

$$\Delta = 4t^2 \cos^2 \theta \sin^2 \theta \left(\frac{1}{b^2} - \frac{1}{a^2} \right)^2 - 4 \left[\frac{\sin^2 \theta}{a^2} + \frac{\cos^2 \theta}{b^2} \right] \left[\frac{t^2 \cos^2 \theta}{a^2} + \frac{t^2 \sin^2 \theta}{b^2} - 1 \right] \quad (48)$$

$$= \frac{4}{a^4 b^4} \left[t^2 \cos^2 \theta \sin^2 \theta (a^2 - b^2)^2 - (b^2 \sin^2 \theta + a^2 \cos^2 \theta) (b^2 t^2 \cos^2 \theta + a^2 t^2 \sin^2 \theta - a^2 b^2) \right] \quad (49)$$

$$= \frac{4}{a^4 b^4} [-2t^2 \cos^2 \theta \sin^2 \theta a^2 b^2 - (a^2 b^2 t^2 \sin^4 \theta - a^2 b^4 \sin^2 \theta + a^2 b^2 t^2 \cos^4 \theta - a^4 b^2 \cos^2 \theta)] \quad (50)$$

$$= \frac{4}{a^2 b^2} [-t^2 (\cos^4 \theta + \sin^4 \theta + 2 \cos^2 \theta \sin^2 \theta) + a^2 \cos^2 \theta + b^2 \sin^2 \theta] \quad (51)$$

$$= \frac{4}{a^2 b^2} [-t^2 (\cos^2 \theta + \sin^2 \theta)^2 + a^2 \cos^2 \theta + b^2 \sin^2 \theta] \quad (52)$$

$$= 4 \frac{a^2 \cos^2 \theta + b^2 \sin^2 \theta - t^2}{a^2 b^2} \quad (53)$$

So finally, the length of the segment support of the radon transform is:

$$\frac{\sqrt{\Delta}}{\left[\frac{\sin^2 \theta}{a^2} + \frac{\cos^2 \theta}{b^2} \right]} = \frac{2\sqrt{a^2 \cos^2 \theta + b^2 \sin^2 \theta - t^2}}{ab \left(\frac{\sin^2 \theta}{a^2} + \frac{\cos^2 \theta}{b^2} \right)} = 2ab \frac{\sqrt{a^2 \cos^2 \theta + b^2 \sin^2 \theta - t^2}}{a^2 \cos^2 \theta + b^2 \sin^2 \theta} \quad (54)$$

So one finally gets:

$$\mathcal{R}_\theta(t) = 2ab \frac{\sqrt{a^2 \cos^2 \theta + b^2 \sin^2 \theta - t^2}}{a^2 \cos^2 \theta + b^2 \sin^2 \theta} \mathbb{1}_{\{t^2 \leq a^2 \cos^2 \theta + b^2 \sin^2 \theta\}}(t) \quad (55)$$

Now the formula for a rotated and translated ellipse can be obtained from it, using two basic properties of the Radon transform:

1. *Rotation:* If $g(r, \theta) = f(r, \theta - \theta_0)$, then

$$\mathcal{R}^g_\theta(t) = \mathcal{R}^f_{\theta-\theta_0}(t) \quad (56)$$

2. *Translation:* If $g(x, y) = f(x - x_0, y - y_0)$, then

$$\mathcal{R}^g_\theta(t) = \mathcal{R}^f_\theta(t - x_0 \cos \theta - y_0 \sin \theta) \quad (57)$$

So using **first** the rotation formula **then** the translation formula, one can get the Radon transform of a rotated and translated ellipse.

Caution: The inverse is not true because the rotation is with respect to the origin, so must be done before the translation.

3.1.3 Fourier slice theorem

Let's now illustrate the Fourier slice theorem in the case of a simple ellipse. By denoting $c := \sqrt{a^2 \cos^2 \theta + b^2 \sin^2 \theta}$, one gets:

$$\hat{\mathcal{R}}_\theta(\omega) = \frac{2ab}{c} \int_{-\infty}^{+\infty} \sqrt{c^2 - t^2} \mathbb{1}_{\{t^2 \leq c^2\}}(t) e^{-i\omega t} dt \quad (58)$$

$$= \frac{2ab}{c^2} \int_{-c}^{+c} \sqrt{c^2 - t^2} e^{-i\omega t} dt \quad (59)$$

$$= \frac{2ab}{c^2} \int_0^{+c} \sqrt{c^2 - t^2} 2 \cos(\omega t) dt \quad (60)$$

$$= 4ab \int_0^1 \sqrt{1 - u^2} \cos(\omega cu) du \quad (61)$$

$$(u = \frac{t}{c}) \quad (62)$$

$$= 4ab \int_0^{\frac{\pi}{2}} \sqrt{1 - \sin^2 \theta} \cos(\omega c \sin \theta) \cos \theta d\theta \quad (63)$$

$$(u = \sin \theta) \quad (64)$$

$$= 4ab \cdot \frac{1}{2} \int_{-\frac{\pi}{2}}^{\frac{\pi}{2}} \sqrt{1 - \sin^2 \theta} \cos(\omega c \sin \theta) \cos \theta d\theta \quad (65)$$

$$= 4ab \cdot \frac{1}{2} \int_0^\pi \sqrt{1 - \sin^2 \theta} \cos(\omega c \sin \theta) \cos \theta d\theta \quad (66)$$

$$= 2ab \int_0^\pi \cos^2 \theta \cos(\omega c \sin \theta) d\theta \quad (67)$$

$$= ab \int_0^\pi (1 + \cos(2\theta)) \cos(\omega c \sin \theta) d\theta \quad (68)$$

$$= ab \int_0^\pi \cos(\omega c \sin \theta) d\theta + \frac{ab}{2} \int_0^\pi \cos(2\theta + \omega c \sin \theta) + \cos(2\theta - \omega c \sin \theta) d\theta \quad (69)$$

$$= ab\pi J_0(\omega c) + \frac{ab}{2}\pi (J_2(\omega c) + J_2(-\omega c)) \quad (70)$$

$$= ab\pi J_0(\omega c) + \frac{ab}{2}\pi \cdot 2 (J_2(\omega c)) \quad (71)$$

$$= ab\pi (J_0(\omega c) + J_2(\omega c)) \quad (72)$$

$$= 2\pi ab \frac{J_1(\omega c)}{\omega c} \quad (73)$$

where the last few lines were obtained using parity of J_2 and a recurrence relation on Bessel functions⁵. We finally get that:

$$\boxed{\hat{\mathcal{R}}_\theta(\omega) = \hat{\rho}_{(a,b)}(\omega \cos \theta, \omega \sin \theta)} \quad (74)$$

which illustrates the Fourier slice theorem.

3.2 Discrete reconstruction

In the real setting, one only retrieves a finite number of Radon transforms, due to a finite number of detectors for the parallel rays at a given angle θ and to a finite number of angles. It results in a discretized radial Fourier coefficients distribution. For a given angle θ , one can then compute the Discrete Fourier Transform of the Radon Transform.

Let us consider a discrete sinogram obtained from a finite number of acquisitions. To set the notations, let us say that we irradiate the patient with a finite number of N regularly spaced angles:

$$\forall n \in \llbracket 0, N-1 \rrbracket, \theta_n = \frac{n\pi}{N} \quad (75)$$

⁵cf. [Wikipedia – Bessel function](#)

and we get a finite number of S parallel line intercepts, corresponding to the different t in the line equations $x \cos \theta + y \sin \theta = t$:

$$\forall k \in \llbracket 0, S-1 \rrbracket, t_k = -1 + \frac{2k}{S} \quad (76)$$

if we assume that the spatial limits of the patient we are imaging are $(-1, 1)$.

The discrete sinogram we get from the acquisition can then be considered as a discrete image:

$$u : \Omega \rightarrow \mathbb{R}; \Omega = \llbracket 0, N-1 \rrbracket \times \llbracket 0, S-1 \rrbracket \quad (77)$$

The discrete tomographic reconstruction considered in that subsection will be the following:

1. Perform the 1D Discrete Fourier Transform (DFT) on the discrete sinogram, angle by angle, to get an approximation for the Radial Fourier Transform at each angle.
2. Perform linear interpolation on the resulting discrete Radial Fourier Transform in order to get Cartesian Fourier coefficients.
3. Perform Inverse Fourier Transform on the interpolated Fourier spectrum to get the reconstructed image.

In the following sub-subsections, we will illustrate and analyze the reconstruction process on a simple opened uniform ellipse, whose parameters are:

$$\begin{cases} x_0 &= 0 \\ y_0 &= 0 \\ a_{ext} &= 0.6 \\ b_{ext} &= 0.9 \\ a_{int} &= 0.54 \\ b_{int} &= 0.81 \\ \theta &= 0 \end{cases} \quad (78)$$

It could represent for instance the skull of a patient.

For the CT reconstruction parameters, we will take:

$$\begin{cases} S &= 512 \\ N &= 25 \end{cases} \quad (79)$$

Remark: A typical coupling of parameters in the real medical setting is $(S = 512, N = 1000)$ ⁶, so our angular discretization is very poor. We did it on purpose in order to really see the angular discretization impact on the reconstruction. We later illustrate the impact of the angular discretization on the reconstruction (cf. Figures 9, 14, 19).

The ellipse under study is illustrated in Figure (3), as well as its analytical Fourier Transform and its sinogram, whose formulas were previously derived. The discrete version of those operators will be considered in the Inverse Crime subsection (3.3), where we apply those discrete operators directly on a discrete version of the phantom, instead of computing them exactly using the analytical formulas.

We recover the oscillations of the Bessel function of the first kind of order 1, modulated by the norm of the spatial variables. The x axis is mapped to a slowly oscillating Bessel function according to the formula, and the y axis to a quicker one. The sinogram is trended in a linear combination of $\sqrt{C^2 - t^2}$ on the horizontal axis, and as a more complex combination of sinusoidal functions on the vertical axis. It gets larger when the ellipse is rotated at an angle of $\frac{\pi}{2}$, because then the ellipse is irradiated in its whole length, whereas it gets thinner but lighter for an angle of 0 as the ellipse is irradiated in its width.

⁶cf. Upstate medical university – CT reconstruction

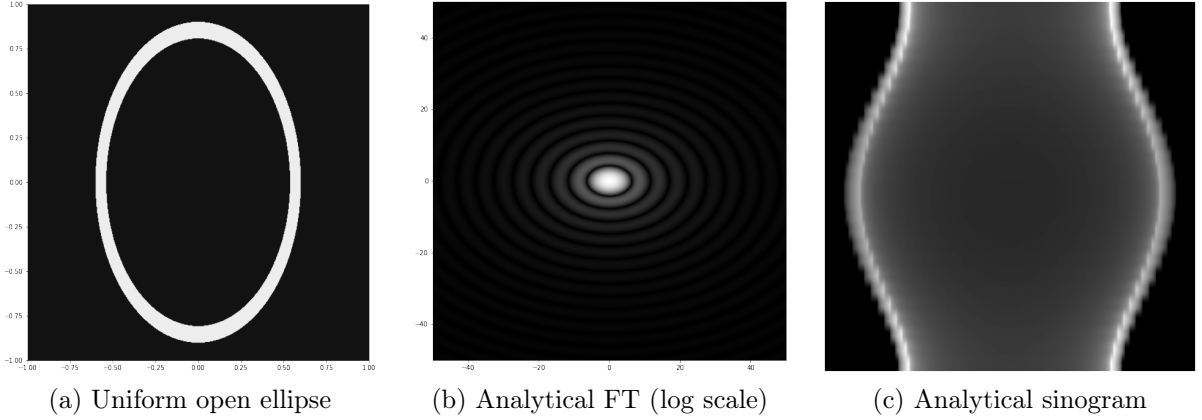


Figure 3: Illustration of the simple uniform elliptical phantom under study in this subsection, as well as its analytical Fourier Transform and sinogram.

3.2.1 Discrete Fourier Transform of the discrete Radon Transform

Then one has, using the formalism of 1D Discrete Fourier Transform for each angle θ_n :

$$\forall p \in \llbracket 0, S - 1 \rrbracket, \hat{u}_n(p) = \sum_{k=0}^{S-1} e^{-i \frac{2\pi p k}{S}} u(n, k) \quad (80)$$

Using the formula (55) for the Radon Transform that we obtained in the previous subsection (for a simple ellipse for clarity, although it could be used as well with the rotated and translated version), we get for every $n \in \llbracket 0, N - 1 \rrbracket$ and $p \in \llbracket 0, S - 1 \rrbracket$:

$$\hat{u}_n(p) = \sum_{k=0}^{S-1} e^{-i \frac{2\pi p k}{S}} \mathcal{R}_{\frac{n\pi}{N}} \left(-1 + \frac{2k}{S} \right) \quad (81)$$

$$= \frac{2ab}{a^2 \cos^2 \left(\frac{n\pi}{N} \right) + b^2 \sin^2 \left(\frac{n\pi}{N} \right)} \sum_{k=0}^{S-1} \sqrt{a^2 \cos^2 \left(\frac{n\pi}{N} \right) + b^2 \sin^2 \left(\frac{n\pi}{N} \right) - \left(-1 + \frac{2k}{S} \right)^2} e^{-i \frac{2\pi p k}{S}} \quad (82)$$

Using Fourier slice theorem, we deduce that those are approximations for the radial Fourier coefficients of the original ellipse.

Then we can compare those coefficients to the original ones for an ellipse. We will do it numerically but we could probably go further and analyze the convergence of the related series to Bessel functions when $S \rightarrow +\infty$.

The Discrete Fourier Transform of the sinogram is illustrated in Figure (4). As a reminder, according to the Fourier Slice theorem, those coefficients approximately correspond to the radial coefficients of the elliptical phantom's Fourier Transform (cf. eq. (5)). In order to map it to a Cartesian grid, we perform a change of coordinates and visualize the radial sinogram's FT on a Cartesian grid on Figure (5).

3.2.2 Interpolation of the radial Discrete Fourier Transform

Now the idea is to perform a radial linear interpolation of the radially distributed discrete Fourier coefficients obtained from the 1D DFT of the discrete sinogram.

The scheme for interpolation is illustrated in Figure (6).

Let us consider a Fourier coefficient $(k_x, k_y) = (\omega \cos \theta, \omega \sin \theta)$. Then there exists a unique couple (ω_k, θ_n) such that:

$$\begin{cases} \omega \in [\omega_p, \omega_{p+1}[\\ \theta \in [\theta_n, \theta_{n+1}[\end{cases} \quad (83)$$

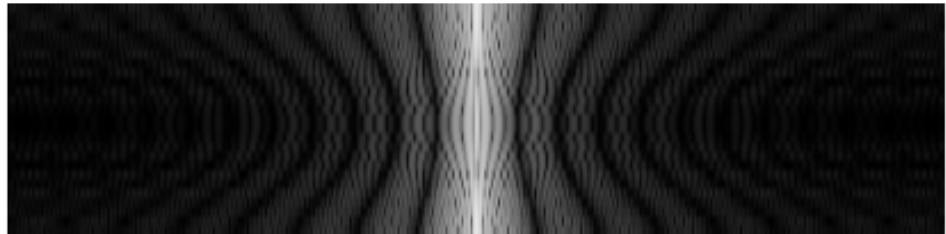


Figure 4: Discrete Fourier Transform of the elliptical phantom's analytical sinogram

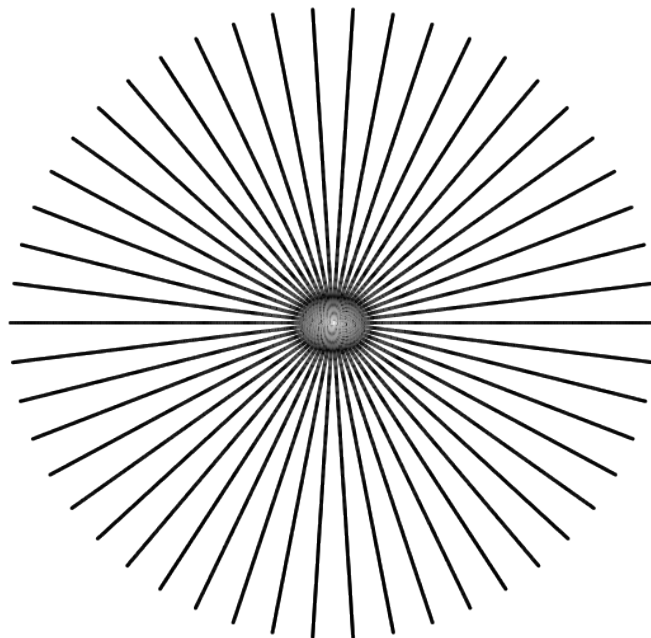


Figure 5: Cartesian visualization of the radial Discrete Fourier Transform of the elliptical phantom's analytical sinogram

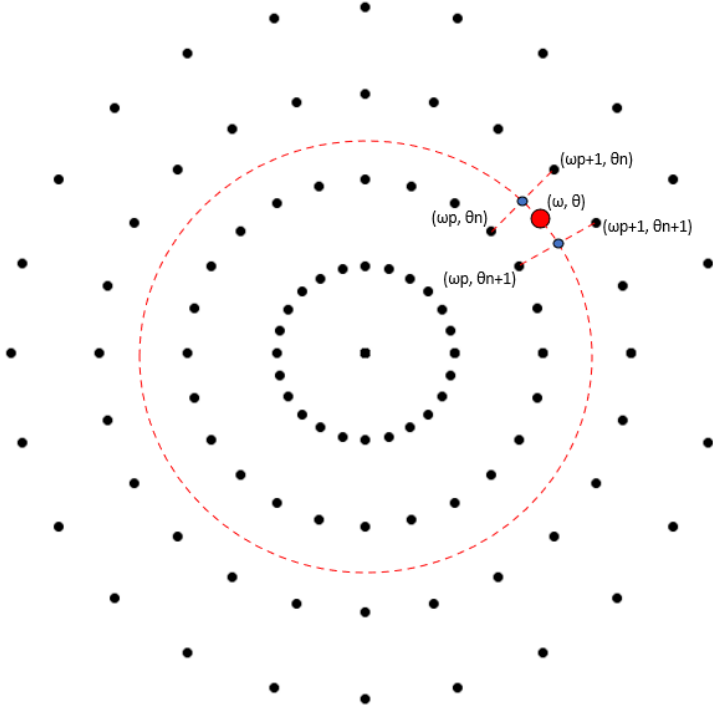


Figure 6: Schema of the radial Fourier Transform interpolation.

Using bi-linear interpolation, one has:

$$\begin{aligned} \hat{u}_{interp}(\omega \cos \theta, \omega \sin \theta) = & \\ & \left(1 - \frac{\theta - \theta_n}{\theta_{n+1} - \theta_n}\right) \left[\left(1 - \frac{\omega - \omega_p}{\omega_{p+1} - \omega_p}\right) \hat{u}(\omega_p \cos \theta_n, \omega_p \sin \theta_n) + \left(\frac{\omega - \omega_p}{\omega_{p+1} - \omega_p}\right) \hat{u}(\omega_{p+1} \cos \theta_n, \omega_{p+1} \sin \theta_n) \right] \\ & + \left(\frac{\theta - \theta_n}{\theta_{n+1} - \theta_n}\right) \left[\left(1 - \frac{\omega - \omega_p}{\omega_{p+1} - \omega_p}\right) \hat{u}(\omega_p \cos \theta_{n+1}, \omega_p \sin \theta_{n+1}) + \left(\frac{\omega - \omega_p}{\omega_{p+1} - \omega_p}\right) \hat{u}(\omega_{p+1} \cos \theta_{n+1}, \omega_{p+1} \sin \theta_{n+1}) \right] \end{aligned}$$

In terms of sinogram index, one has:

$$\begin{aligned} \hat{u}_{interp}(\omega \cos \theta, \omega \sin \theta) = & \\ & \left(1 - \frac{\theta - \theta_n}{\theta_{n+1} - \theta_n}\right) \left[\left(1 - \frac{\omega - \omega_p}{\omega_{p+1} - \omega_p}\right) \hat{u}_n(p) + \left(\frac{\omega - \omega_p}{\omega_{p+1} - \omega_p}\right) \hat{u}_n(p+1) \right] \\ & + \left(\frac{\theta - \theta_n}{\theta_{n+1} - \theta_n}\right) \left[\left(1 - \frac{\omega - \omega_p}{\omega_{p+1} - \omega_p}\right) \hat{u}_{n+1}(p) + \left(\frac{\omega - \omega_p}{\omega_{p+1} - \omega_p}\right) \hat{u}_{n+1}(p+1) \right] \end{aligned}$$

Finally, the closed form expression for the p and n such that $\omega \in [\omega_p, \omega_{p+1}[; \theta \in [\theta_n, \theta_{n+1}[$ is:

$$\begin{cases} \omega \in [\omega_p, \omega_{p+1}[\iff \omega \in \left[-1 + \frac{2p}{S}, -1 + \frac{2(p+1)}{S}\right] \iff p = \left\lfloor \frac{(\omega+1)S}{2} \right\rfloor \implies \omega_p = -1 + \frac{2}{S} \left\lfloor \frac{(\omega+1)S}{2} \right\rfloor \\ \theta \in [\theta_n, \theta_{n+1}[\iff \theta \in \left[\frac{n\pi}{N}, \frac{(n+1)\pi}{N}\right] \iff n = \left\lfloor \frac{\theta N}{\pi} \right\rfloor \implies \theta_n = \frac{\left\lfloor \frac{\theta N}{\pi} \right\rfloor \pi}{N} \end{cases} \quad (84)$$

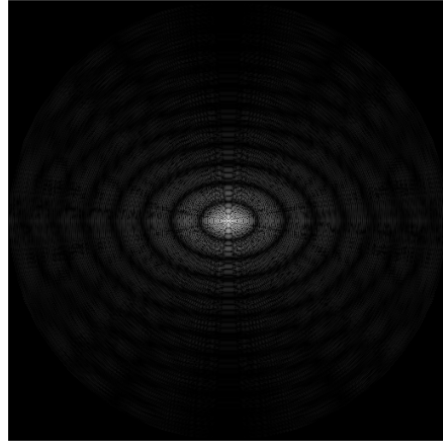


Figure 7: Interpolation of the radial Discrete Fourier Transform of the elliptical phantom's analytical sinogram.

$$\begin{aligned}
 \hat{u}_{\text{interp}}(\omega \cos \theta, \omega \sin \theta) = & \\
 & \left(1 - \frac{\theta - \lfloor \frac{\theta N}{\pi} \rfloor \pi}{\frac{\pi}{N}} \right) \\
 & \left[\left(1 - \frac{\omega + 1 - \frac{2}{S} \lfloor \frac{(\omega+1)S}{2} \rfloor}{\frac{2}{S}} \right) \hat{u}_{\lfloor \frac{\theta N}{\pi} \rfloor} \left(\left\lfloor \frac{(\omega+1)S}{2} \right\rfloor \right) + \left(\frac{\omega + 1 - \frac{2}{S} \lfloor \frac{(\omega+1)S}{2} \rfloor}{\frac{2}{S}} \right) \hat{u}_{\lfloor \frac{\theta N}{\pi} \rfloor} \left(\left\lfloor \frac{(\omega+1)S}{2} \right\rfloor + 1 \right) \right] \\
 & + \left(\frac{\theta - \lfloor \frac{\theta N}{\pi} \rfloor \pi}{\frac{\pi}{N}} \right) \\
 & \left[\left(1 - \frac{\omega + 1 - \frac{2}{S} \lfloor \frac{(\omega+1)S}{2} \rfloor}{\frac{2}{S}} \right) \hat{u}_{\lfloor \frac{\theta N}{\pi} \rfloor + 1} \left(\left\lfloor \frac{(\omega+1)S}{2} \right\rfloor \right) + \left(\frac{\omega + 1 - \frac{2}{S} \lfloor \frac{(\omega+1)S}{2} \rfloor}{\frac{2}{S}} \right) \hat{u}_{\lfloor \frac{\theta N}{\pi} \rfloor + 1} \left(\left\lfloor \frac{(\omega+1)S}{2} \right\rfloor + 1 \right) \right]
 \end{aligned}$$

The linear interpolation of the radial Discrete Fourier Transform is illustrated in Figure (7). It should be an approximation of the Fourier Transform of the ellipse, which was illustrated in Figure (3). We however notice the presence of "crosses" that are characteristic of the discontinuity of the Discrete Fourier Transform, that assumes the periodicity of the sinogram signal as explained in [Moisan 2011]. Fortunately, those crosses have rather low intensity, which can be explained by the fact that the image sinogram is pretty "dark" at the borders, and this is not necessarily due to the simplicity of our phantom, but rather to the fact that X-rays won't be attenuated by the environment around the imaged patient (mostly air), so even in the real setting, the sinogram shouldn't have large discontinuities at the borders, and the reconstruction using the DFT of the sinogram shouldn't be that much impacted by the discontinuities. However, we notice here that there are other artifacts in this interpolated Fourier Transform, due to the process of CT-reconstruction, when compared to the analytical FT of the ellipse. Indeed the isolines of the Bessel function look noisy, and most particularly we notice a small elliptical noise along the vertical axis. This might be caused both by the radial bi-linear interpolation and the discretization of the sinogram, that looks pretty noisy due to the small angular resolution during acquisition.

3.2.3 Inverse Fourier Transform of the interpolated Fourier spectrum

Finally in order to recover the approximated original image, we use the Inverse Fourier Transform on the previously obtained formula, using a prior polar change of coordinates.

$$\begin{aligned}
u(x, y) &= \int_{-\infty}^{+\infty} \int_{-\infty}^{+\infty} \hat{u}(k_x, k_y) e^{-i(k_x, k_y) \cdot (x, y)} dk_x dk_y \\
&= \int_{-\infty}^{+\infty} \int_0^{\pi} \hat{u}(\omega \cos \theta, \omega \sin \theta) e^{-i\omega[x \cos \theta + y \sin \theta]} \omega d\omega d\theta \\
&= \int_{-\infty}^{+\infty} \int_0^{\pi} e^{-i\omega[x \cos \theta + y \sin \theta]} \left(1 - \frac{\theta - \lfloor \frac{\theta N}{\pi} \rfloor \pi}{\frac{\pi}{N}} \right) \\
&\quad \left[\left(1 - \frac{\omega + 1 - \frac{2}{S} \lfloor \frac{(\omega+1)S}{2} \rfloor}{\frac{2}{S}} \right) \hat{u}_{\lfloor \frac{\theta N}{\pi} \rfloor} \left(\left\lfloor \frac{(\omega+1)S}{2} \right\rfloor \right) + \left(\frac{\omega + 1 - \frac{2}{S} \lfloor \frac{(\omega+1)S}{2} \rfloor}{\frac{2}{S}} \right) \hat{u}_{\lfloor \frac{\theta N}{\pi} \rfloor} \left(\left\lfloor \frac{(\omega+1)S}{2} \right\rfloor + 1 \right) \right] \\
&\quad + e^{-i\omega[x \cos \theta + y \sin \theta]} \left(\frac{\theta - \lfloor \frac{\theta N}{\pi} \rfloor \pi}{\frac{\pi}{N}} \right) \\
&\quad \left[\left(1 - \frac{\omega + 1 - \frac{2}{S} \lfloor \frac{(\omega+1)S}{2} \rfloor}{\frac{2}{S}} \right) \hat{u}_{\lfloor \frac{\theta N}{\pi} \rfloor + 1} \left(\left\lfloor \frac{(\omega+1)S}{2} \right\rfloor \right) + \left(\frac{\omega + 1 - \frac{2}{S} \lfloor \frac{(\omega+1)S}{2} \rfloor}{\frac{2}{S}} \right) \hat{u}_{\lfloor \frac{\theta N}{\pi} \rfloor + 1} \left(\left\lfloor \frac{(\omega+1)S}{2} \right\rfloor + 1 \right) \right] \omega d\omega d\theta
\end{aligned}$$

One could then develop the sum expression for the DFT of u , invert the sum and the integral, and check if there are some interesting properties on the resulting series, which will not *a priori* lead to a close form formula. For instance, one could study whether the support of such a function is also an ellipse, or where does it change, and study the influence of the discretization step on the support of the function. Maybe by pushing N and S to $+\infty$ we could recover the exact support of an ellipse.

We illustrate the reconstruction results on Figure (8). The reconstruction is pretty faithful to reality in the sense that the shape of the ellipse is recovered. However, it is pretty noisy, and one can imagine that it could lead to more serious artifacts for a more complex phantom, with smaller details. Here we can notice two kinds of artifacts, some mid-frequency noise inside the ellipse, that does not harm that much the understanding of the shape, and some outer mid-frequency noise, that looks like rotated residuals of the ellipse. The second one could have a more important impact on a complex phantom, as it could artificially disturb the surrounding of an organ and create some artifacts that could lead to misdiagnosis. Fortunately, the rather periodic nature of that noise makes it rather detectable and possibly even correctable in post-processing. The first kind of noise, inside the ellipse, is not very problematic in our case of a uniform ellipse, but could reveal more important in the real setting, where the organs are not uniform at all, and it could be interesting to study more complex non-uniform phantoms in a later work, to study the impact of the discretization steps on the noise in those non-uniform organs.

Finally, we illustrate the reconstruction results for several angle values in Figure (9). As we can notice, the reconstruction becomes pretty accurate for $N \geq 50$.

3.3 Inverse Crime

Now to finish the analysis of such a reconstruction process, we wanted to study the situation of inverse crime. As a reminder, the inverse crime situation in inverse problems happens when we use the same object both for simulation and reconstruction. In our case of tomographic reconstruction, the inverse crime would consist, instead of using a sinogram obtained from a simulated continuous phantom, using the closed-form expression we derived above, in using directly a discrete version of the input continuous phantom, and extract its sinogram using continuous operations like rotation and translation on the discrete image. A classical way to extract the sinogram from a rasterized image is to first perform an interpolation, then perform a rotation on the continuous image, then discretize it again, and finally compute the sum over each line.

Let us consider an ellipse of axes (a, b) with $a < 1, b < 1$ so that the support of the related continuous image I is in $\Omega = [-1, 1]^2$. Let us consider as well as a discretization of size (L, L) of the image, I^d . One has:

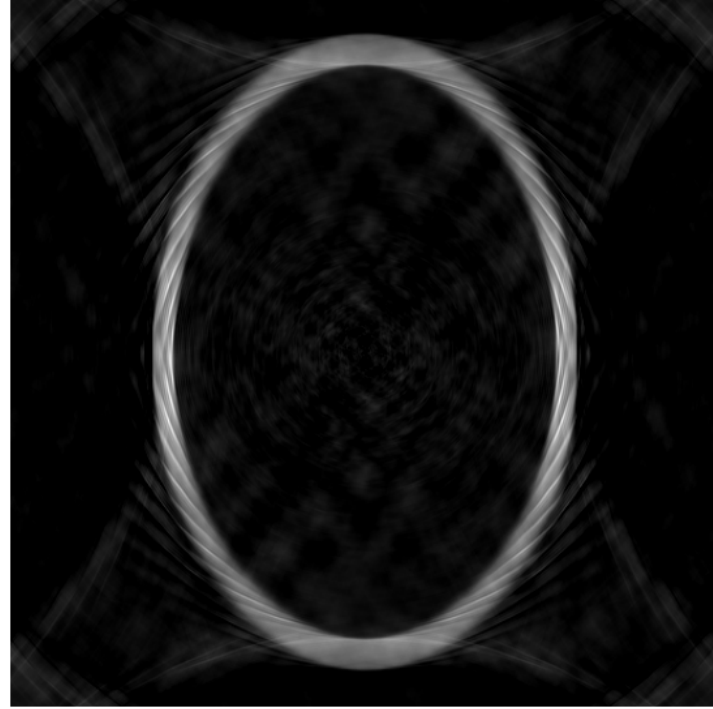


Figure 8: CT reconstruction of the open ellipse, with $N = 25; S = 512$

$$I^d(k, l) = \begin{cases} 1 & \text{if } \left(\frac{-1+\frac{2k}{L}}{a}\right)^2 + \left(\frac{-1+\frac{2l}{L}}{b}\right)^2 \leq 1 \\ 0 & \text{otherwise} \end{cases} \quad (85)$$

The linear interpolation of that discrete ellipse yields:

$$I^c(x, y) = \left(1 - \frac{x-k}{\frac{2}{L}}\right) \left(1 - \frac{y-l}{\frac{2}{L}}\right) I^d(k, l) + \frac{x-k}{\frac{2}{L}} \left(1 - \frac{y-l}{\frac{2}{L}}\right) I^d(k+1, l) + \frac{y-l}{\frac{2}{L}} \left(1 - \frac{x-k}{\frac{2}{L}}\right) I^d(k, l+1) + \frac{x-k}{\frac{2}{L}} \frac{y-l}{\frac{2}{L}} I^d(k+1, l+1)$$

with

$$\begin{cases} k &= \left\lfloor \frac{(x+1)L}{2} \right\rfloor \\ l &= \left\lfloor \frac{(y+1)L}{2} \right\rfloor \end{cases} \quad (86)$$

The rotation of angle θ given by the matrix $R(\theta) = \begin{pmatrix} \cos(\theta) & -\sin(\theta) \\ \sin(\theta) & \cos(\theta) \end{pmatrix}$ on the continuous image is:

$$I^c \circ R(\theta)^{-1}(x, y) = I^c(x \cos \theta + y \sin \theta, -x \sin \theta + y \cos \theta) \quad (87)$$

And its discretization of size (L, L) is:

$$I^d \circ R(\theta)^{-1}(k, l) = I^c \circ R(\theta)^{-1} \left(-1 + \frac{2k}{L}, -1 + \frac{2l}{L}\right) \quad (88)$$

Finally, the discrete sinogram, which is the sum of the intensities over each line is:

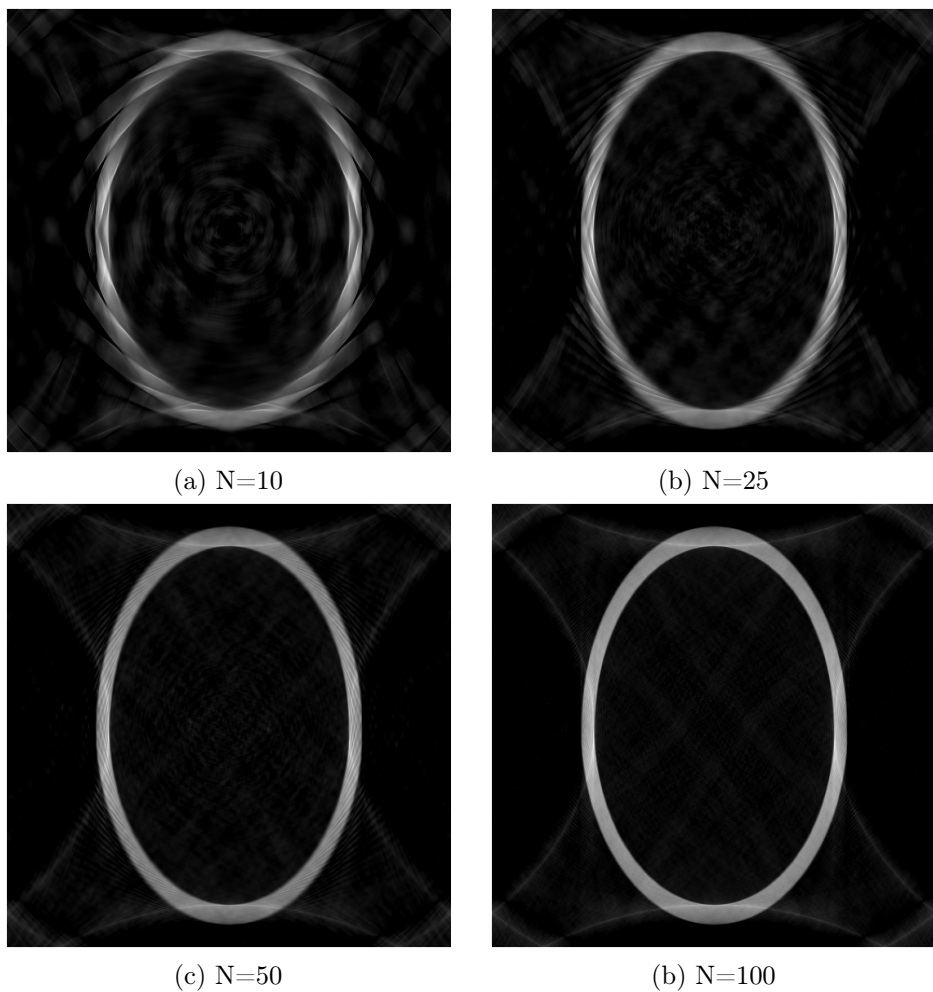


Figure 9: Impact of the angular discretization on the reconstruction of a simple open elliptical phantom

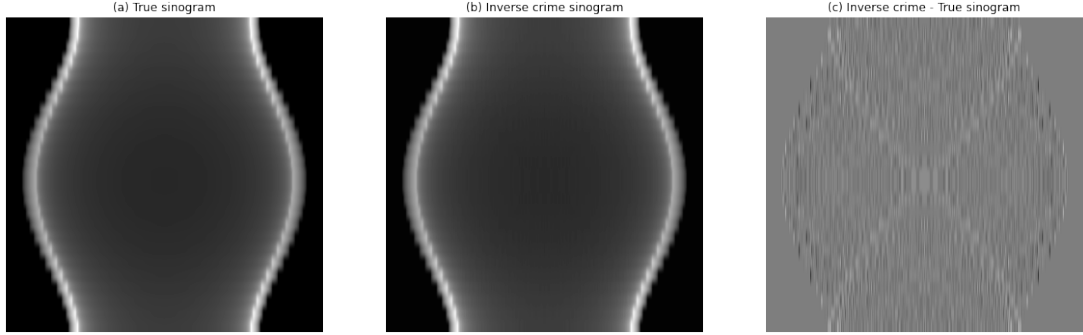


Figure 10: Comparison of the sinograms obtained with or without committing an inverse crime.

$$\mathcal{R}_\theta(k) = \sum_{l=1}^L I^d \circ R(\theta)^{-1}(k, l) \quad (89)$$

$$\mathcal{R}_\theta(k) = \sum_{l=1}^L I^c \circ R(\theta)^{-1} \left(-1 + \frac{2k}{L}, -1 + \frac{2l}{L} \right) \quad (90)$$

$$\mathcal{R}_\theta(k) = \sum_{l=1}^L I^c \left(\left(-1 + \frac{2k}{L} \right) \cos \theta + \left(-1 + \frac{2l}{L} \right) \sin \theta, \left(1 - \frac{2k}{L} \right) \sin \theta + \left(-1 + \frac{2l}{L} \right) \cos \theta \right) \quad (91)$$

Same as before, one could develop more the formulas to study the impact of the rasterized image discretization step on the sinogram, when compared to the discrete sinogram obtained from the true continuous image $\mathcal{R}_{\frac{n\pi}{N}}(-1 + \frac{2k}{S})$. Our intuition is that in the case of uniform ellipses, with bi-linear interpolation for the rotation, we don't lose that much information about the presence of an object on the sinogram when committing an inverse crime. The shape won't be very faithful to reality, but it should be globally preserved. With Shannon interpolation on non-uniform ellipses, however, this inverse-crime situation could have more important consequences.

We illustrate the inverse crime situation in Figure (10), where we compare the sinogram obtained with the analytical formula of the Radon Transform to the one obtained by performing an interpolation, then a rotation, then a sampling, and then a sum, hence committing an inverse crime. The two sinograms are pretty close in that case (the high resolution of the rasterized image (512×512) might help). However, we notice interestingly a "rounded X-shaped" difference between the two sinograms, that corresponds to the ray crossing the ellipse along the x-axis. The sampling of the ellipse, combined with a linear interpolation, a rotation and another sampling might create a niche effect, particularly pronounced along the long axis of the ellipse, whose low curvature might be down-sampled to a line when committing inverse-crime.

The reconstruction result under the inverse crime situation is illustrated in Figure (11). The difference is minimal, probably due to the thin discretization, however if we look more closely, the inverse crime elliptical reconstruction is a bit more noisy inside the ellipse. It might be due to the aliasing that happens when sampling from the discontinuous elliptical phantom.

3.4 Results on more complex phantoms

Now we illustrate the results on more complex phantoms. The first examples were done on a simple ellipse, without rotation nor translation. This one could represent the skull of an imaged patient. We will first reproduce the process with a rotated and translated ellipse, that is smaller and could represent a tiny tumor in a brain that we want to detect. Then we will use the linearity of the operators involved in the CT reconstruction process (Radon Transform and Fourier Transform) and perform the CT reconstruction of a more complex phantom.

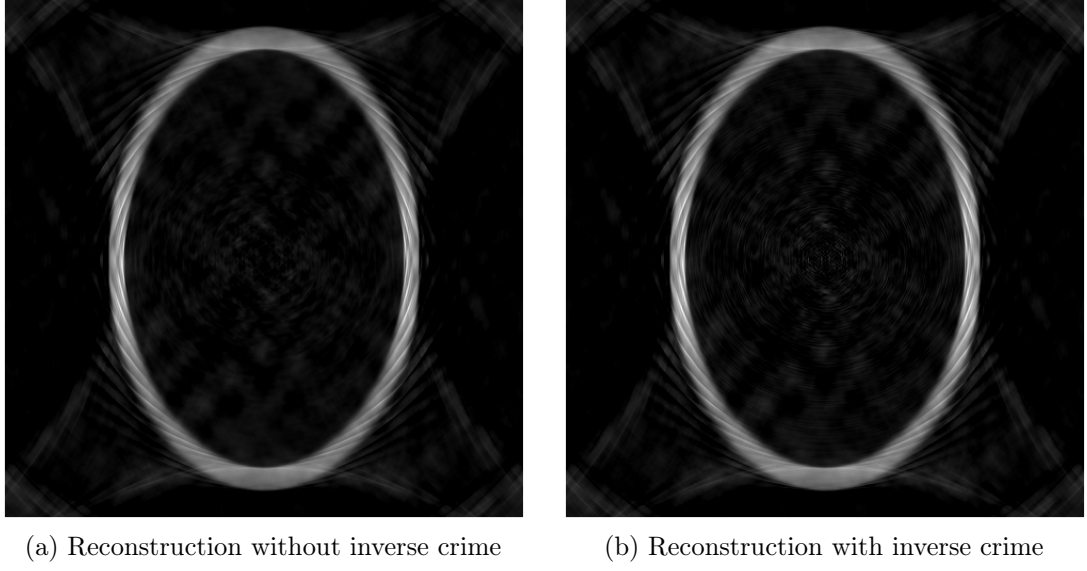


Figure 11: Comparison between the elliptical phantom reconstruction within the regular and inverse crime frameworks

3.4.1 Tiny rotated and translated ellipse

In this sub-subsection, we illustrate and analyze the reconstruction process on a tiny rotated and translated ellipse, that could represent a tumor in the brain that we want to detect and whose parameters are:

$$\begin{cases} x_0 = -0.15 \\ y_0 = -0.2 \\ a = 0.1 \\ b = 0.12 \\ \theta = \frac{\pi}{6} \end{cases} \quad (92)$$

For the CT reconstruction parameters, we used the same parameters as before.

The ellipse under study is illustrated in Figure (12), as well as its analytical Fourier Transform and its sinogram, whose formulas were previously derived. As expected, the Fourier Transform is visually obtained by rotating and then inverting the axes in the image domain. The sinogram is no longer symmetric with respect to the y axis due to the translation.

The reconstruction is illustrated in Figure (13). It looks pretty faithful, especially given the small size of the original object, which illustrates the potential for the reconstruction of small shapes like cancerous cells boundaries. However, let us not forget that the surrounding ellipses might cause outside noise, thus potentially impacting the tumor if it is close to a large ellipse, like the skull.

The reconstruction with different angular discretizations is illustrated in Figure (14). For $N \geq 50$, the reconstruction looks pretty qualitative.

The inverse crime situation is illustrated in Figures (15, 16). This time, there is no obvious difference pattern due to the inverse crime, like the "rounded X-shaped" curve in (10). We can notice once again that the reconstruction is pretty more qualitative using the true analytical sinogram; indeed, we can notice some stripes inside the tumor in the inverse crime situation.

3.4.2 Complex phantom as a combination of ellipses

In this sub-subsection, we illustrate and analyze the reconstruction process on a more complex phantom using the linearity in the operators involved in the CT reconstruction. We designed a phantom that could

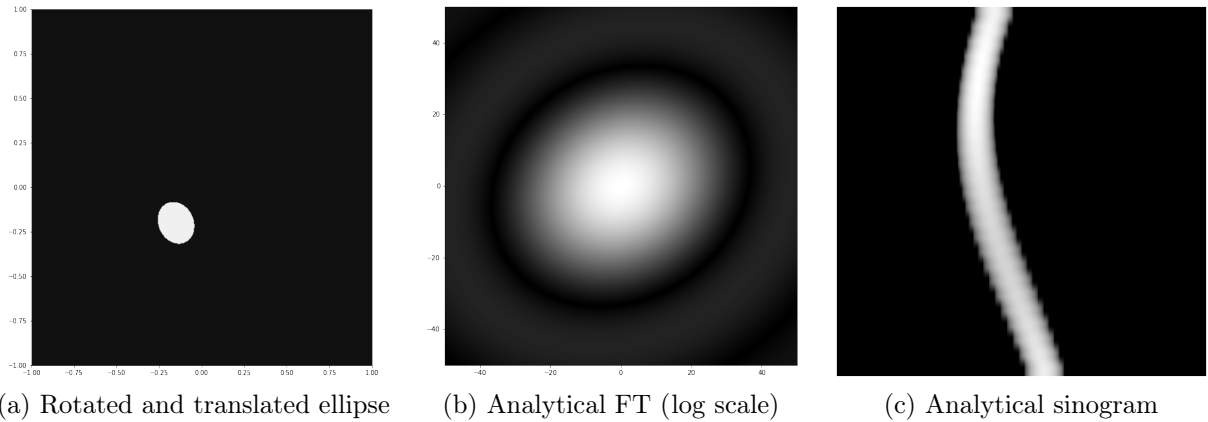


Figure 12: Illustration of the uniform rotated and translated elliptical phantom under study, as well as its analytical Fourier Transform and sinogram.

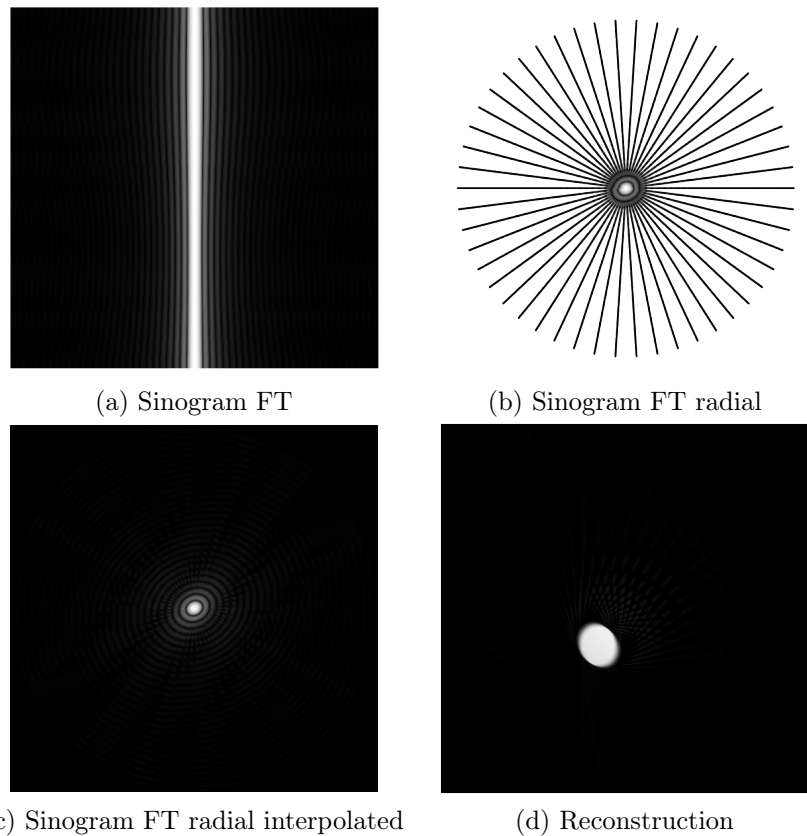


Figure 13: CT reconstruction of the uniform rotated and translated elliptical phantom under study.

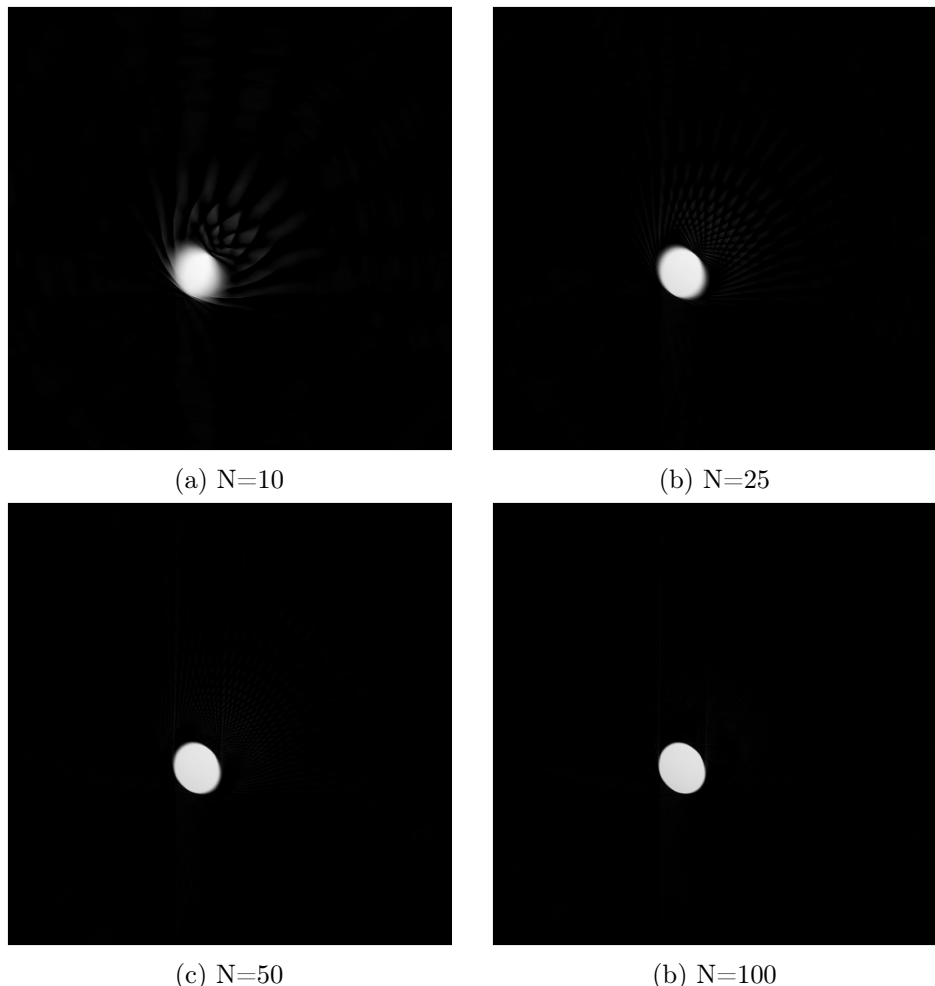


Figure 14: Impact of the angular discretization on the reconstruction of the rotated and translated elliptical phantom

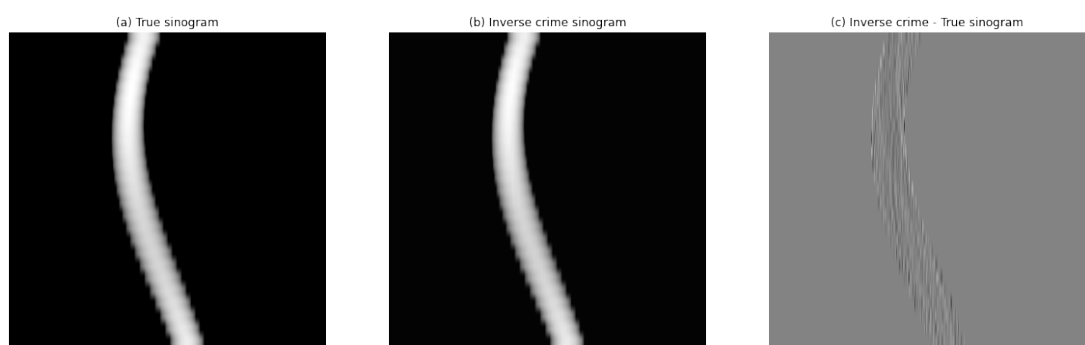


Figure 15: Comparison of the sinograms obtained with or without committing an inverse crime.

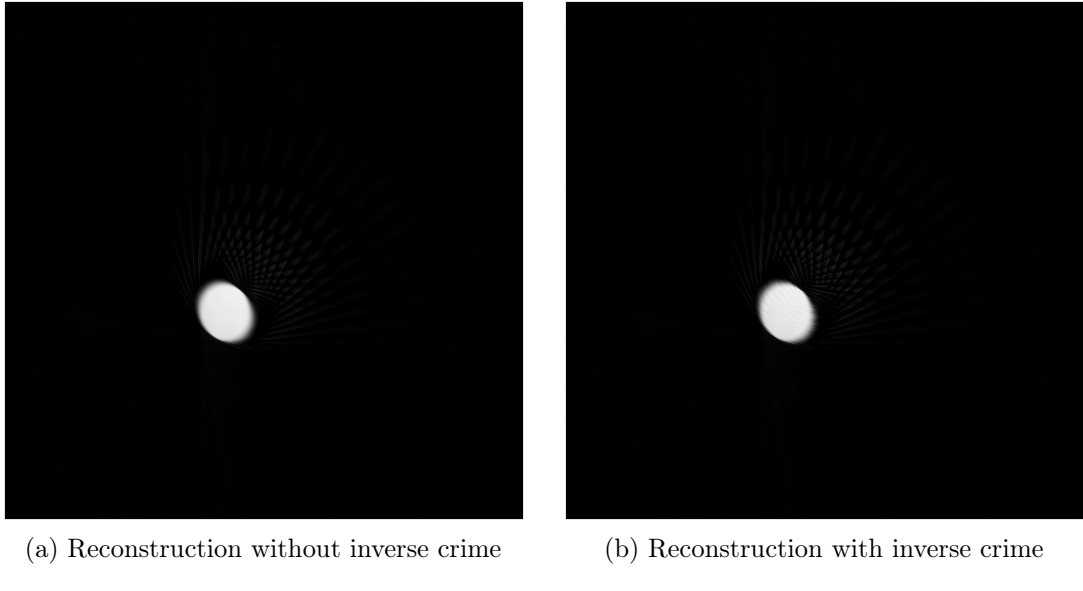


Figure 16: Comparison between the rotated and translated elliptical phantom reconstruction within the regular and inverse crime frameworks.

ρ	x_0	y_0	a	b	θ
5	0	0	0.6	0.9	0
-5	0	0	0.54	0.81	0
2	-0.15	-0.2	0.1	0.12	$\frac{\pi}{6}$
1	-0.2	-0.2	0.23	0.25	$-\frac{\pi}{20}$
1	-0.2	0	0.2	0.6	$-\frac{\pi}{20}$
1	0.25	0.05	0.2	0.6	$+\frac{\pi}{20}$

Table 1: Parameters for the full elliptical phantom

represent a patient's head with a tiny tumor in it. Different organ densities ρ are involved here. All the parameters of the ellipses are listed in the Table (1).

For the CT reconstruction parameters, we used the same parameters as before.

The phantom under study is illustrated in Figure (17), as well as its analytical Fourier Transform and its sinogram, whose formulas were previously derived. Given the high density of the skull and the linearity of Fourier and Radon Transforms, its trend is predominant in the FT and sinogram plots. However we can still see well the other component's trend in the sinogram.

The reconstruction is illustrated in Figure (18). It is pretty more noisy than previous experiments, due to the exterior noise that intersects with the interior of the other ellipses. However the shapes are well recovered.

The reconstruction with different angular discretizations is illustrated in Figure (19). The image isn't interpretable for $N = 10$. The contours become pretty sharp for $N \geq 100$, with still a bit of noise.

The inverse crime situation is illustrated in Figures (20, 21).

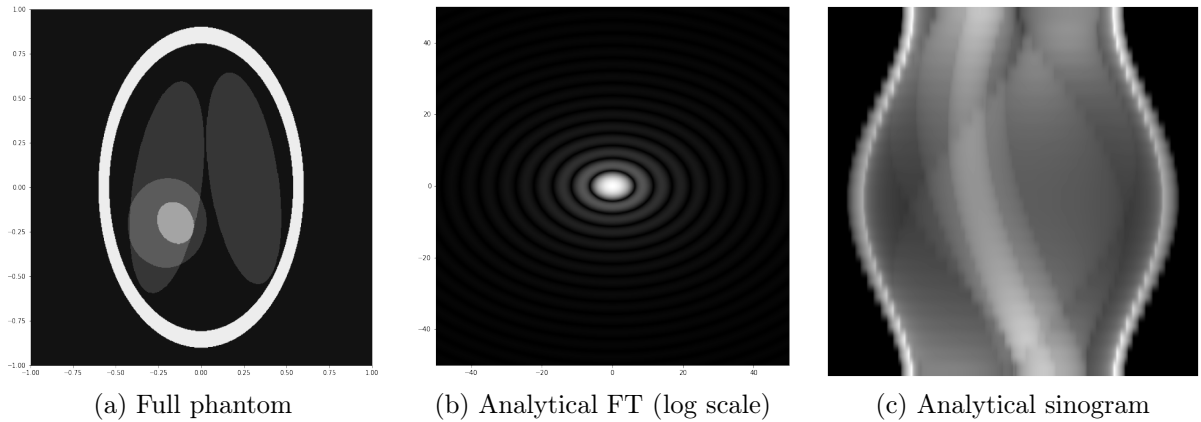


Figure 17: Illustration of the full phantom under study, as well as its analytical Fourier Transform and sinogram.

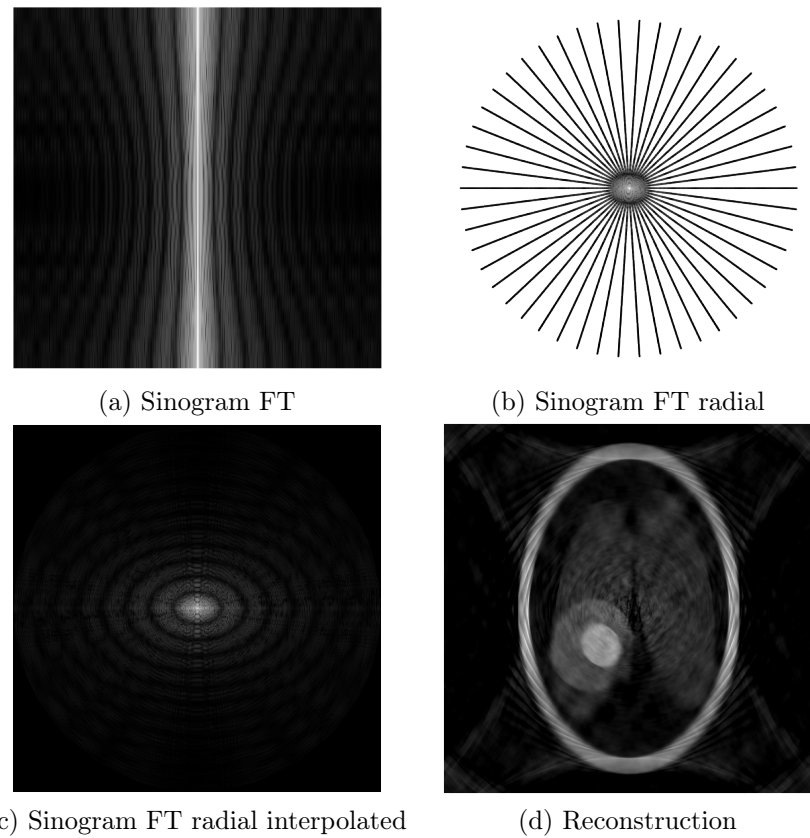


Figure 18: CT reconstruction of the full phantom under study.

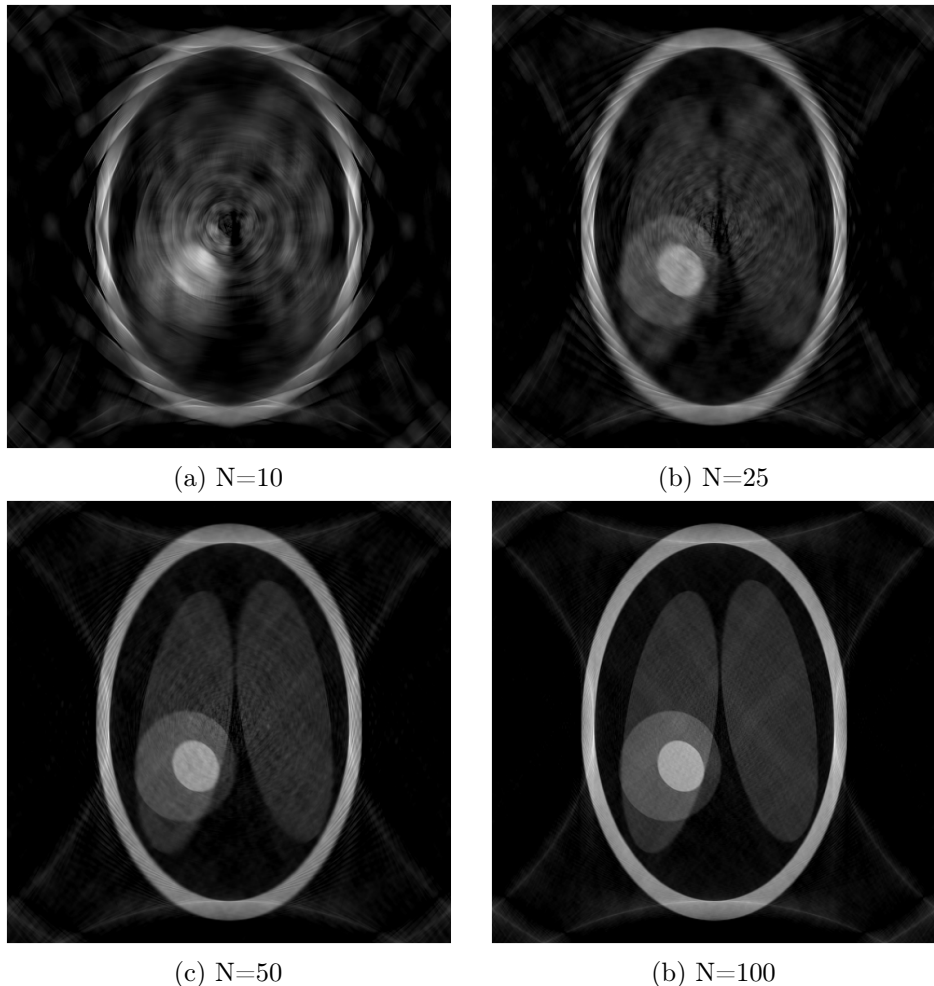


Figure 19: Impact of the angular discretization on the reconstruction of the full phantom.

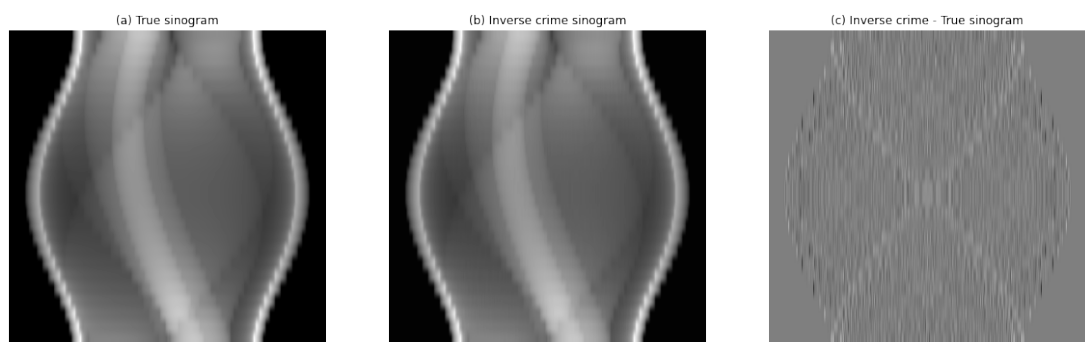


Figure 20: Comparison of the sinograms obtained with or without committing an inverse crime for the full phantom.

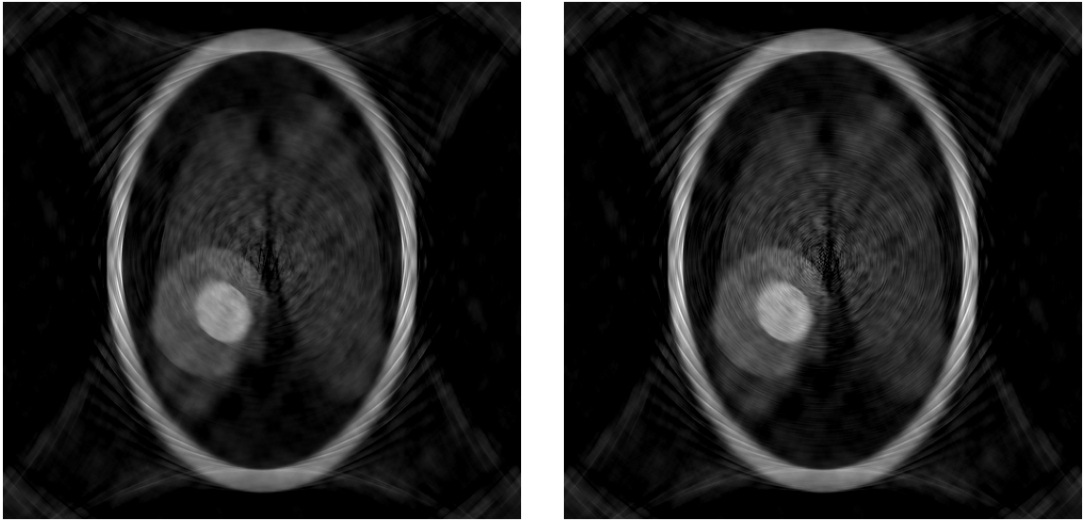


Figure 21: Comparison between the full phantom reconstruction within the regular and inverse crime frameworks.

4 Conclusion and perspectives

In this paper, we proposed an introductory study on the interest of analytical models for phantoms in medical imaging and most particularly for Computed Tomography reconstruction. We saw that phantoms are of paramount importance in medical image reconstruction in order to perform simulations and study the impact of the image acquisition parameters (angular discretization notably) on the quality of the reconstruction. For that we introduced a bi-dimensional phantom composed of several rotated and translated ellipses. Thanks to the properties of the operators involved in the CT reconstruction method, we could limit our study to a single ellipse. The relative simplicity of the expression of such an elliptical phantom allowed us to derive closed-form formulas for its Fourier and Radon Transforms – involving Bessel and sinusoidal functions – and to verify the Fourier Slice theorem that states that the Fourier Transform of the Radon Transform of an object corresponds to the radial coefficients of the Cartesian Fourier Transform of the original object. Thanks to those formulas, we could then formally analyze the CT reconstruction process, that consists in the irradiation of a patient under several discrete angles, yielding a finite number of discrete Radon Transforms, whose Discrete Fourier Transform is then computed and interpolated to recover, via Inverse Fourier Transform, an approximation of the original imaged object. The formulas were this time more complex and without a closed form *a priori*. As a consequence, we implemented them on Python to illustrate the reconstruction process and numerically analyze the impact of the angular discretization on the reconstruction quality. The reconstructions were pretty faithful in terms of shape, although increasingly noisy as the angular discretization decreases. Another aspect that we analyzed is the inverse crime situation, in which the same rasterized image is used both for simulation (extraction of the sinogram with discrete Radon Transform) and reconstruction, yielding sometimes overly optimistic results due to aliasing when sampling a discontinuous image like a phantom representing brain structures. We formulated the situation and derived a formula for the inverse crime sinogram, computed using previous interpolation of the rasterized image. As the formulas were also complex, we decided to analyze the situation numerically as well, and noticed some deterioration of the quality of the reconstruction in the inverse crime situation.

The analytical formulas derived for the CT reconstruction raise interesting perspectives in terms of analysis of the impact of the discretization steps on the quality of the reconstruction. Indeed, with those formulas only, one should be able to analyze the convergence of the discrete scheme to the continuous one when the discretization steps get close to 0. In the case of uniform ellipses, one could study the variation

of the reconstruction's support (to a threshold) with the step size to see how much the imaged structure is deformed by the CT reconstruction. The angular noise outside the ellipse when the angular step is large, which looks like a potential serious obstacle to the faithful reconstruction of detailed structures, could also be possibly analyzed with those formulas. With this analytical work, some maximal discretization steps, depending on the minimal object we want to retrieve (for example a 1 mm³ tumor), could possibly be derived. Finally, our uniform elliptical model is pretty simple and could be further developed, using some non-uniform densities, that remain simple enough to get closed-form formulas; *a priori*, the knowledge of a primitive of the density function should be sufficient to express the Radon Transform formula in closed form.

References

- Abergel, Rémy and Lionel Moisan (Oct. 2017). "The Shannon Total Variation". In: *Journal of Mathematical Imaging and Vision* 59. DOI: [10.1007/s10851-017-0733-5](https://doi.org/10.1007/s10851-017-0733-5).
- Brown, Robert et al. (Apr. 2014). *Magnetic Resonance Imaging: Physical Principles and Sequence Design: Second Edition*. ISBN: 978-0-471-72085-0. DOI: [10.1002/9781118633953](https://doi.org/10.1002/9781118633953).
- Colton, David and Rainer Kress (1992). "Inverse Acoustic and Electromagnetic Scattering Theory". In: Guerquin-Kern, Matthieu et al. (2012). "Realistic Analytical Phantoms for Parallel Magnetic Resonance Imaging". In: *IEEE Transactions on Medical Imaging* 31, pp. 626–636.
- Herman, Gabor T. (2009). "Fundamentals of Computerized Tomography: Image Reconstruction from Projections". In: *Advances in Pattern Recognition*.
- Kak, A.C. and M. Slaney (2001). *Principles of Computerized Tomographic Imaging*. Classics in Applied Mathematics. Society for Industrial and Applied Mathematics. ISBN: 9780898714944. URL: https://books.google.fr/books?id=Z6RpVjb9%5C_lwC.
- Koay, Cheng Guan, Joelle E. Sarlls, and Evren Özarslan (2007). "Three-dimensional analytical magnetic resonance imaging phantom in the Fourier domain". In: *Magnetic Resonance in Medicine* 58.2, pp. 430–436. DOI: <https://doi.org/10.1002/mrm.21292>. eprint: <https://onlinelibrary.wiley.com/doi/pdf/10.1002/mrm.21292>. URL: <https://onlinelibrary.wiley.com/doi/abs/10.1002/mrm.21292>.
- Moisan, Lionel (Feb. 2011). "Periodic Plus Smooth Image Decomposition". In: *Journal of Mathematical Imaging and Vision* 39. DOI: [10.1007/s10851-010-0227-1](https://doi.org/10.1007/s10851-010-0227-1).
- Pruessmann, Klaas P. et al. (1999). "SENSE: Sensitivity encoding for fast MRI". In: *Magnetic Resonance in Medicine* 42.5, pp. 952–962. DOI: [https://doi.org/10.1002/\(SICI\)1522-2594\(199911\)42:5<952::AID-MRM16>3.0.CO;2-S](https://doi.org/10.1002/(SICI)1522-2594(199911)42:5<952::AID-MRM16>3.0.CO;2-S). eprint: <https://onlinelibrary.wiley.com/doi/pdf/10.1002/%28SICI%291522-2594%28199911%2942%3A5%3C952%3A%3AAID-MRM16%3E3.0.CO%3B2-S>. URL: <https://onlinelibrary.wiley.com/doi/abs/10.1002/%28SICI%291522-2594%28199911%2942%3A5%3C952%3A%3AAID-MRM16%3E3.0.CO%3B2-S>.
- Radon, Johann (1986). "On the determination of functions from their integral values along certain manifolds". In: *IEEE Transactions on Medical Imaging* 5.4, pp. 170–176. DOI: [10.1109/TMI.1986.4307775](https://doi.org/10.1109/TMI.1986.4307775).
- Ripoll, Olivier, Ville Kettunen, and Hans Herzig (Sept. 2002). "Low-data simulation of diffractive optical elements based on the zones geometry". In: *Journal of Modern Optics* 49. DOI: [10.1080/09500340210140524](https://doi.org/10.1080/09500340210140524).
- Rudin, Leonid I., Stanley Osher, and Emad Fatemi (1992). "Nonlinear total variation based noise removal algorithms". In: *Physica D: Nonlinear Phenomena* 60.1, pp. 259–268. ISSN: 0167-2789. DOI: [https://doi.org/10.1016/0167-2789\(92\)90242-F](https://doi.org/10.1016/0167-2789(92)90242-F). URL: <https://www.sciencedirect.com/science/article/pii/016727899290242F>.
- Shepp, LA et al. (1980). "Computerized tomography and nuclear magnetic resonance". In: *J. Comput. Assist. Tomogr* 4.1, pp. 94–107.
- Shepp, Larry A. and Benjamin F. Logan (1974). "The Fourier reconstruction of a head section". In: *IEEE Transactions on Nuclear Science* 21, pp. 21–43.